Chemical Engineering Journal 504 (2025) 158966

Contents lists available at ScienceDirect

Chemical Engineering Journal

journal homepage: www.elsevier.com/locate/cej

Ultrafast synthesis of vanadium-based oxides with crystalline-amorphous heterostructure for advanced aqueous zinc-ion batteries

Duan Yan [a], Hanbo Li [a], Aomen Yang [a], Menglian Wang [a], Kaiqi Nie [b], Xiaoxin Lv [a,*], Jiujun Deng [a,*]

[a] Institute for Energy Research, Automotive Engineering Research Institute, Jiangsu University, 301 Xuefu Road, Zhenjiang 212013, China
[b] Institute of High Energy Physics, Chinese Academy of Sciences, Beijing 100049, China

ARTICLE INFO

Keywords:
Amorphous
Vanadium
Heterostructure
Cathode
Zinc-ion batteries
Flash Joule heating

ABSTRACT

The development of amorphous-crystalline hybrids shows significant promise for high-performance cathodes in aqueous zinc ion batteries (ZIBs). However, efficient and controlled synthesis remains a major challenge due to the thermodynamic instability of amorphous materials. In this study, we present a facile and ultrafast method for the controlled fabrication of crystalline V_2O_3 and amorphous sodium vanadate (V_2O_3/a-NVO) heterostructure using the flash Joule heating technique, achieved in approximately 3 s. Benefitting from abundant storage sites and isotropic charge transfer channel of a-NVO, as well as the intimate contact between V_2O_3 and a-NVO, the resulting heterostructure exhibits significant pseudocapacitive contribution and accelerated reaction kinetics, further facilitated by the co-insertion of H^+/Zn^{2+}. This results in impressive electrochemical performance, with a high specific capacity of 414.6 mAh/g at 0.2 A/g and a capacity of 329.2 mAh/g at a current density of 1 A/g after 1000 cycles. Notably, it retains a high capacity of 138 mAh/g after 5000 cycles at a large current density of 10 A/g. This approach offers a facile and rapid strategy for designing efficient vanadium-based oxide cathodes through the rational design of amorphous-crystalline heterostructures.

1. Introduction

Aqueous rechargeable batteries have garnered significant attention as alternative systems to lithium-ion batteries (LIBs) due to their high ionic conductivity (≈ 0.1–1 S cm^{-1}), enhanced safety, and environmental benignity of aqueous electrolytes [1–5]. Amongst, aqueous zinc ion batteries (ZIBs) stand out for their potential on account of advantageous properties of Zn metal anode, including high theoretical capacity (820 mAh/g), low redox potential of Zn^{2+}/Zn (−0.76 V versus standard hydrogen electrode), excellent chemical stability in water, and abundance [3–7]. Recent efforts have focused on the development of efficient cathodes, as the high polarization property of Zn^{2+} can result in strong electrostatic interactions with cathode materials, severely hindering storage kinetics [5–7]. Among various cathode materials, vanadium-based oxides such as V_2O_5, VO_2, and V_2O_3, along with vanadates (such as metal vanadates and ammonium vanadates) have emerged as promising candidates [8–10]. Their layered and tunnel structures, combined with the multiple oxidation states of vanadium (+2 to + 5), endow superior storage abilities [8–10]. However, these cathodes also suffer from intrinsic drawbacks such as poor electric conductivity, sluggish kinetics, dissolution of active materials, and structural collapse, leading to poor cycling stability and low rate capability [8–10].

To address these issues, diverse strategies such as morphological design, disorder engineering, metal atoms doping, and the integration of conductive substances have been exploited to improve the electrochemical performance of vanadium-based oxide cathodes [8–10]. Amongst, the building of amorphous-crystalline hybrids has proven to be a valid route and has gained significant attention [11,12]. As reported in the literature, different from crystalline counterparts, the amorphous phase with a disordered structure can break the space constraints to obtain open frameworks, which can not only provide more storage sites and isotropic ions diffusion channels for facilitating ion insertion but also accommodate the lattice strain to greatly minimize the structural changes during the cycling, achieving the boosted cycling stability [13]. Simultaneously, the highly symmetrical, rigid structure of the crystalline phase can improve the electrode's conductivity and contribute to a more stable structure during repeated ion insertion and extraction processes

* Corresponding authors.
E-mail addresses: xxlv@ujs.edu.cn (X. Lv), jjDeng@ujs.edu.cn (J. Deng).

https://doi.org/10.1016/j.cej.2024.158966
Received 23 October 2024; Received in revised form 20 December 2024; Accepted 24 December 2024
Available online 25 December 2024

[11,14,15]. However, it is important to note that amorphous materials are generally thermodynamically unstable, necessitating precise experimental control during the synthesis of crystalline-amorphous heterostructures. [16,17]. Therefore, developing facile and controlled synthesis strategies for crystalline-amorphous heterostructures is crucial for obtaining efficient vanadium-based oxide cathodes [15].

Recently, the flash Joule heating as a novel synthetic technique has attracted increasing interest since its ability to achieve a high temperature (up to ~ 3000 °C) at ultrafast heating and cooling rates (up to ~ 10^5 K/s), which are orders of magnitude larger than those of conventional furnace calcination [18–20]. This unique characteristic enables the synthesis more facile and efficient by greatly reducing both time and energy consumption while simultaneously suppressing the structure aggregation of materials at an elevated temperature [18–20]. As a result, flash Joule heating has been extensively utilized to rapidly fabricate a variety of functional materials, including nanocarbon and its composite [21,22], high-entropy alloys [23], single-atom catalysts [24], and metastable materials [25,26]. In terms of crystalline-amorphous heterostructures, flash Joule heating has shown great potential for facile, efficient, and controlled synthesis. Its extremely rapid heating and quenching rates could effectively suppress the undesired but thermodynamically favorable amorphous-to-crystalline transition [16,17]. Nevertheless, the application of flash Joule heating for fabricating efficient amorphous-crystalline heterostructure cathodes has been scarcely explored.

In this study, we present a facile and ultrafast method for the controlled fabrication of crystalline V_2O_3 and amorphous sodium vanadate heterostructure (labeled as V_2O_3/a-NVO) using the flash Joule heating technique, which takes approximately 3 s. Electrochemical measurements demonstrate that on account of rich storage sites and isotropic ions diffusion channels of a-NVO, alongside the intimate contact between crystalline V_2O_3 and a-NVO, the resulting heterostructure delivers significant pseudocapacitive contributions and accelerated reaction kinetics. Moreover, the resulting heterostructure undergoes a distinctive mechanism of proton insertion accompanied by Zn-ion storage through the reversible deposition of $Zn_4(OH)_6SO_4{\cdot}5H_2O$, further enhancing the charge dynamics. Eventually, the V_2O_3/a-NVO heterostructure exhibits remarkable electrochemical performance, achieving a high specific capacity of 414.6 mAh/g at 0.2 A/g and a capacity of 329.2 mAh/g at a current density of 1 A/g after 1000 cycles. Notably, it retains a high capacity of 138 mAh/g after 5000 cycles at a large current density of 10 A/g. This work provides a facile and cost-effective strategy for designing efficient vanadium-based oxide cathodes through the rational design of amorphous-crystalline heterostructures.

2. Experimental section

2.1. Sample preparation

For the synthesis of V_2O_3/a-NVO heterostructure, a sodium vanadate sample was first prepared by treating the commercial V_2O_5 powder in NaCl aqueous solution [27,28]. Briefly, 2 g of commercial V_2O_5 powder (99.99 %, Rhawn, Shanghai, China) was dispersed in 100 ml of 2 M NaCl (Sinopharm Chemical Reagent Co., Ltd., China) aqueous solution, and stirred at room temperature for 72 h. Following this, the solution was centrifuged to separate the solids, which were then washed several times with deionized (DI) water and dried in a vacuum oven at 60°C overnight. Next, urea (Sinopharm Chemical Reagent Co., Ltd., China) was mixed with the sodium vanadate sample in weight ratios of 2:1, 1:1, and 1:2. After grinding, 500 mg of the mixture was placed onto graphite paper and sealed in a quartz tube with ceramic plugs. The ends of the graphite paper were then connected to the copper contacts of the flash Joule heating furnace (Hefei In-situ High-tech Co., Ltd.). Finally, the V_2O_3/a-NVO composite was successfully synthesized through an ultrafast heating/quenching process using a quick model with an input voltage of 15 V, an input current of 150 A, and a heating temperature of ~ 1600 °C, followed by washing with DI water. For samples annealed at ~ 1200 °C and 2000 °C, the electrical parameters were 20 V, 140 A, and 30 V, 200 A, respectively. For comparison, the VO_2/NVO sample was synthesized using the same procedure as the V_2O_3/a-NVO heterostructure, but without the addition of the urea precursor.

2.2. Structural characterization

The morphologies of as-obtained samples were investigated by using scanning Electron Microscopy (SEM, Quanta FEG 250, FEI) and high-resolution Transmission Electron Microscopy (HRTEM, JEOL 2100F, 200 keV) equipped with energy-dispersive X-ray spectroscopy (EDX, Oxford Instruments Inc.). X-ray Diffraction (XRD) with a copper (Cu) Kα source (Shimadzu XRD-6000) and X-ray Photoelectron Spectroscopy (XPS, Thermo Scientific K-Alpha) were utilized to explore the crystal and electronic structure of the resulting samples, respectively. Thermogravimetric analysis (TGA) ranging from room temperature to 800 °C was conducted in an air atmosphere at a heating rate of 10 °C min^{-1} using Netzsch TGA 209 F1. Raman spectra of the resulting samples were characterized on Thermo Scientific DXR. X-ray absorption spectroscopy (XAS) characterizations were performed at Beamline 4B9B, Beijing Synchrotron Radiation Facility.

2.3. Electrochemical measurements

The electrochemical performance was characterized using CR2025 coin-type cells, comprising the working electrode (cathode), Zn foil (anode), glass fiber (separator), and electrolyte (3 M $Zn(CF_3SO_3)_2$). The working electrode was fabricated by mixing the resulting samples with acetylene black and poly (vinylidene fluoride, PVDF) in a mass ratio of 7:2:1 in N-methylpyrrolidone (NMP) solvent, followed by pasting the slurry onto titanium foil and dried in a vacuum oven at 80°C overnight. The galvanostatic discharge–charge (GCD) curves were collected using LAND CT3001A battery test systems in a voltage window of 0.2–1.6 V. Cyclic voltammetry (CV) and electrochemical impedance spectroscopy (EIS) from 100 kHz to 10 mHz were conducted on an electrochemical workstation (Ivium Vertex. C).

3. Results and discussion

Recently, we demonstrated the rapid fabrication of layer-stacked vanadium oxide/graphene hybrids by sintering commercial V_2O_5 powder on graphite paper using the flash Joule heating strategy [22]. Due to the low melting point of V_2O_5 (~681 °C), the carbothermal shock enabled the commercial V_2O_5 powder to melt, aggregate, and partially reduce into the layer-stacked VO_2/V_2O_5 microstructure. Simultaneously, the melting V_2O_5 detached graphene-like carbon nanosheets from the underlying graphite paper into the resulting samples. However, the micrometer-scale dimensions of the layer-stacked VO_2/V_2O_5 heterostructure required prolonged activation time to achieve high specific capacity. Hence, in this work, the NaCl-treated V_2O_5 nanobelts (sodium vanadate) with smaller sizes are used as the precursor to minimize aggregation into large microstructures to eliminate the need for a prolonged activation process. As shown in Fig. 1, for the synthesis of the V_2O_3/a-NVO heterostructure, sodium vanadate nanobelt bundles ($Na_2V_2O_{16}$, as indexed in XRD patterns in Fig. 1c) were first prepared by stirring commercial V_2O_5 powders in a NaCl solution for 72 h at room temperature, promoting the dissolution of bulk V_2O_5 and the subsequent recrystallization of dissolved VO_x species [27,28]. The resulting sodium vanadate sample was then mixed with urea precursor and sealed in a quartz glass tube for high-temperature sintering using flash Joule heating equipment. During this process, an instantaneous current pulse was applied to the graphite paper substrate, reaching a high temperature of approximately 1600 °C in about 0.3 s, followed by rapid quenching in about 2.7 s (total time: ~3 s, Fig. S1). As demonstrated in Fig. 1b, this

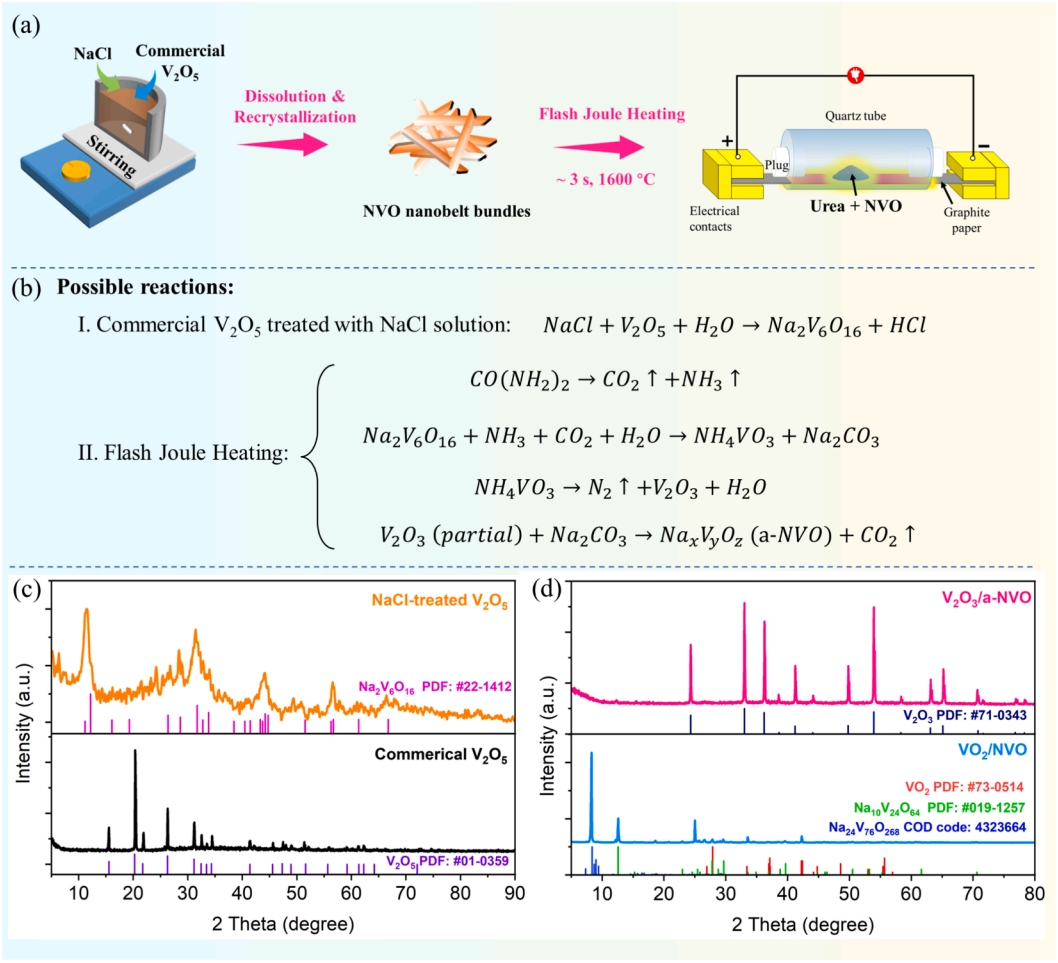

Fig. 1. (a) Schematic illustration and (b) possible reactions for the fabrication of V_2O_3 /a-NVO heterostructure; XRD patterns (c, d) for the commercial V_2O_5 and NaCl-soaked V_2O_5 (c), and V_2O_3 /a-VNO and VO_2 /NVO samples (d).

carbothermal shock could induce the rapid pyrolysis of urea (the decomposition temperature of ~ 130 °C) to release a large amount of CO_2 and NH_3 gas, which then underwent multi-step reactions with the sodium vanadate to generate a heterostructure composed of crystallized V_2O_3 (PDF#71–0343, Fig. 1d) and amorphous sodium vanadate (NVO). These preferential reactions mitigate the detachment of the graphite paper and the introduction of carbon nanosheets into the heterostructure. In contrast, the absence of the urea precursor in the VO_2/NVO sample resulted in a composition primarily of crystalline VO_2 and crystalline sodium vanadate ($Na_{10}V_{24}O_{64}$ and $Na_{24}V_{76}O_{268}$), as indicated by the XRD pattern in Fig. 1d.

Fig. 2 presents scanning electron microscopy (SEM) images of the resulting samples. It is clear that after the soaking treatment in NaCl aqueous solution, the commercial V_2O_5 powder transforms from micrometer-sized particles (Fig. 2a) into nanobelt bundles (Fig. 2b). Subsequently, after the flash Joule heating treatment, these nanobelt bundles slightly melt into the nanosheet-like morphology (Fig. 2c), which has been observed in the VO_2/NVO sample (Fig. S2). Further, high-resolution transmission electron microscopy (HRTEM) characterizations were performed to explore the subtle structure of the resulting samples. As shown in Fig. 2d and Fig. 2e, a hybrid structure consisting of crystallized V_2O_3 and amorphous sodium vanadate is observed in the V_2O_3/a-NVO sample. The lattice spacing of 0.27 nm corresponding to the (104) plane of V_2O_3 strongly suggests the good crystalline of V_2O_3 nanostructures [29]. Additionally, HRTEM images have revealed the intimate contact between a-NVO and crystalline V_2O_3, which will be beneficial for greatly facilitating charge transfer in the resulting heterostructure. Fig. 2f displays the elemental mappings of the V_2O_3/a-NVO heterostructure, revealing a uniform distribution of O, V, and Na atoms.

The electronic structure and elemental composition of the resulting samples were characterized by performing X-ray photoelectron spectroscopy (XPS) and X-ray absorption spectra (XAS) measurements. As shown in Fig. S3a, the XPS survey spectra of the V_2O_3/a-NVO and VO_2/NVO samples clearly reveal the presence of C 1 s, O 1 s, V 2p, and Na 1 s peaks. The weaker C 1 s peak in the V_2O_3/a-NVO heterostructure rules out the possibility of carbon residues originating from urea decomposition and/or detachment of the graphite paper substrate. This conclusion is further supported by Raman characterizations (Fig. S4), which show the presence of V-O and Na-O bonds without the characteristic D and G peaks of carbon-based materials (at approximately 1300 and 1600 cm^{-1}, respectively) in the V_2O_3/a-NVO heterostructure. Fig. 3a illustrates the high-resolution Na 1 s spectrum of the V_2O_3/a-NVO heterostructure, where a binding energy of 1071 eV indicates that Na atoms are bound to oxygen (Na-O bond). The V 2p XPS spectrum in Fig. 3b reveals two prominent peaks at 516.5 and 523.9 eV, corresponding to V $2p_{3/2}$ and V $2p_{1/2}$, respectively [30,31]. The spectrum also reveals the presence of V^{5+}, V^{4+}, and V^{3+}, which result from crystalline V_2O_3 and amorphous NVO components in the heterostructure [30,31]. In contrast, no V^{3+} signal is detected in the high-resolution V 2p XPS spectrum of the VO_2/NVO composite (Fig. S3d), indicating the different components in both samples. Relative to XPS, XAS is a more powerful tool to provide deeper insights into the electronic structure of matter [32,33]. Thus, XAS measurements were subsequently conducted to probe the local

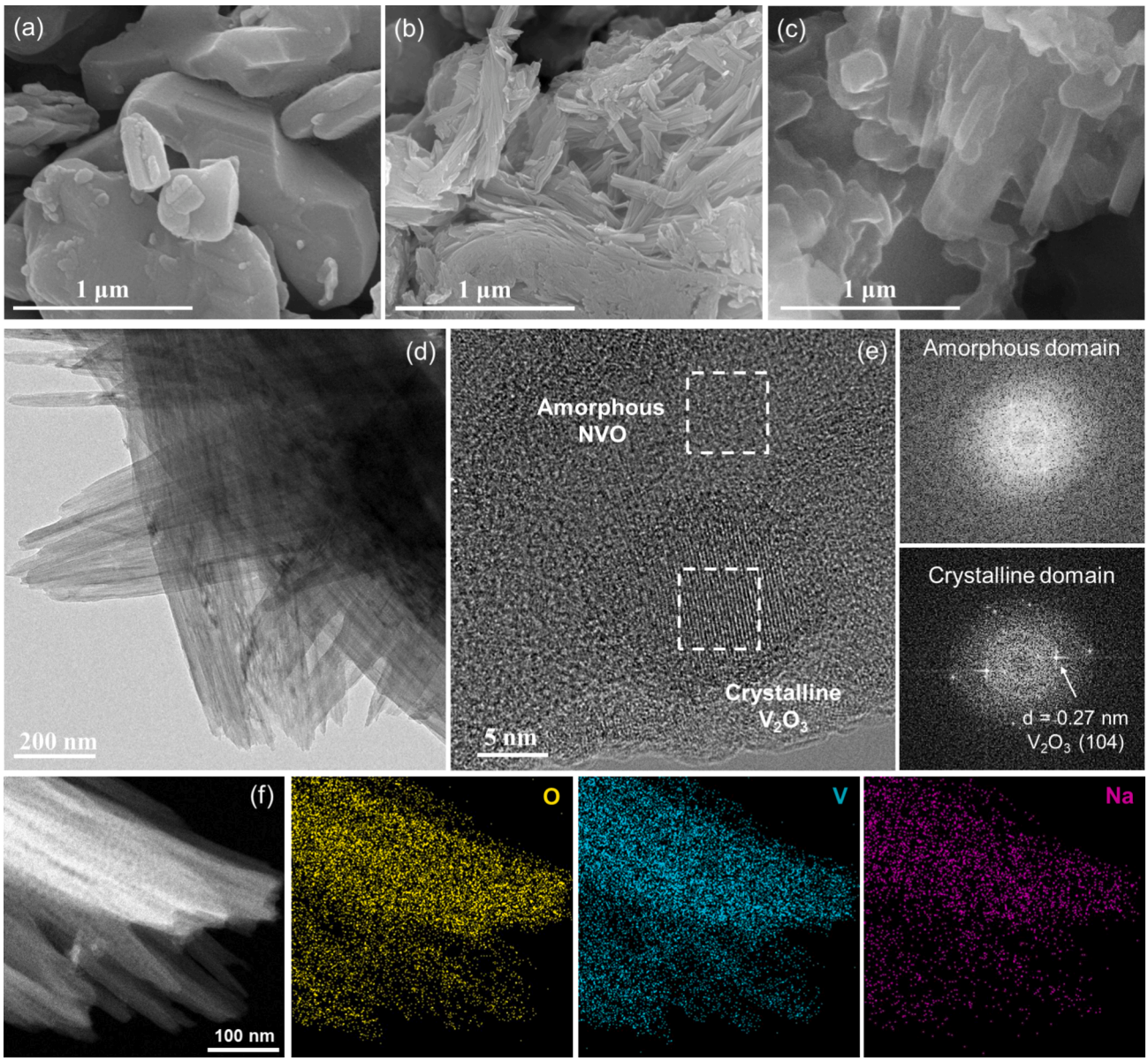

Fig. 2. SEM images of the commercial V_2O_5 (a) and after the treatment of NaCl solution (b) and the as-resulting V_2O_3 /a-NVO heterostructure (c); HRTEM images (d, e) and the corresponding FFT patterns and elemental mappings (f) of V_2O_3 /a-NVO heterostructure.

structure of the V_2O_3/a-NVO heterostructure in more detail. Fig. 3c presents the V L-edge XAS spectra for the V_2O_3/a-NVO heterostructure and V_2O_3 and $Na_{0.33}V_2O_5$ references. It demonstrates that the chemical states of vanadium in the V_2O_3/a-NVO sample are most likely a mixture of those of V_2O_3 and NVO. Fig. 3d shows the O K-edge XAS spectra for the V_2O_3/a-NVO heterostructure and $Na_{0.33}V_2O_5$ reference, where peaks A and B can be assigned to the hybridization of O 2p states with V t_{2g}* and e_g* states [34,35]. Similar to the V L-edge XAS, the O K-edge spectrum of the V_2O_3/a-NVO heterostructure exhibits mixed spectral features from the V_2O_3 and $Na_{0.33}V_2O_5$ reference [34,35]. All these results evidence the successful construction of crystalline V_2O_3 and amorphous NVO heterostructure. Subsequently, thermogravimetric analysis (TGA) characterizations were conducted to determine the contents of V_2O_3 and NVO in the resulting composite. As displayed in Fig. S5, a significant weight increase of about 18.84 % is observed, attributed to the transformation of V_2O_3 to V_2O_5 in the air atmosphere. It reveals that the weight ratios of the V_2O_3 and amorphous NVO components in the resulting composite are approximately 88.2 % and 11.8 %, respectively.

The electrochemical performance of the resulting sample as a cathode for ZIBs was evaluated by assembling a coin cell with a Zn foil anode, 3 M $Zn(CF_3SO_3)_2$ electrolyte, and a glass fiber separator. Fig. 4a shows the cyclic voltammetry (CV) curves of the V_2O_3/a-NVO cathode over the initial 3 cycles at a scan rate of 0.1 mV/s. Two oxidation peaks at ~ 1.30 and ~ 1.40 V are observed in the first cycle, differing significantly from those in subsequent cycles. Previous studies suggest that this behavior may result from the decomposition of water molecules (proton insertion) and/or the electrochemical oxidation of V_2O_3 [36,37]. After the 15th cycle, the CV curves overlap (Fig. 4b), indicating good reversibility of Zn^{2+} storage in the V_2O_3/a-NVO cathode. Additionally, there are two pairs of redox peaks at ~ 1.02/0.89 V and ~ 0.71/0.52 V, corresponding to the transition of V^{5+}/V^{4+} and V^{4+}/V^{3+}, respectively, associated with the multistep Zn^{2+} intercalation/deintercalation process [38,39]. Fig. S6 shows the cycling performance and galvanostatic charge–discharge (GCD) curves for the V_2O_3/a-NVO cathode at a low current density of 0.2 A/g, in which a high capacity retention rate of about 82 % is achieved after 100 cycles. Furthermore, the GCD profiles at this current density exhibit stable plateaus with

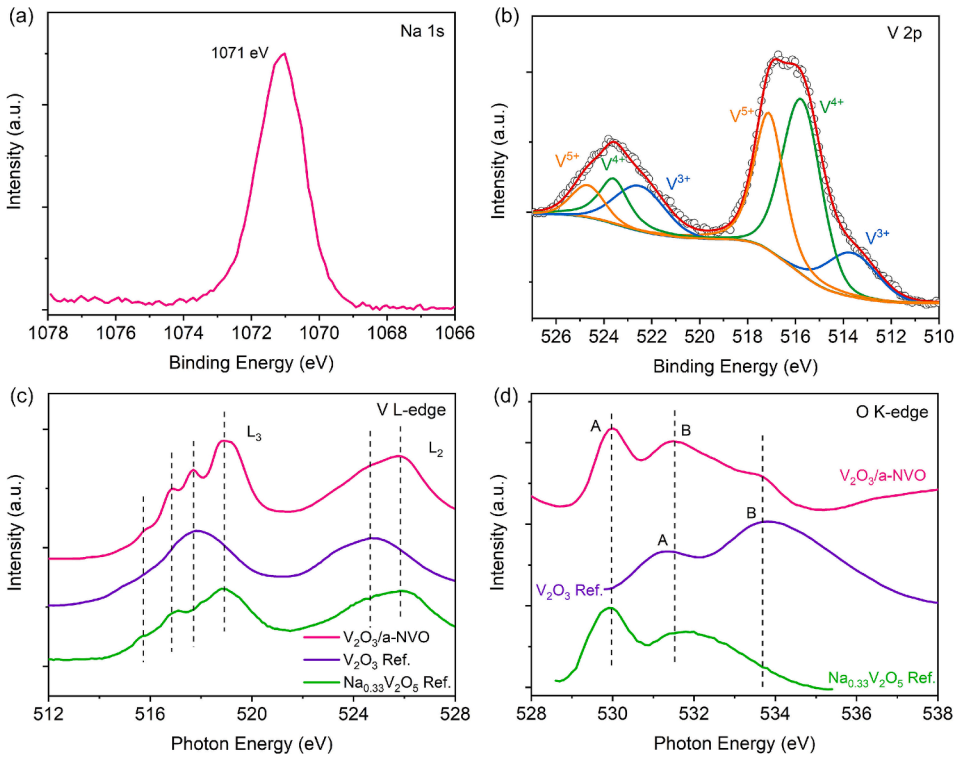

Fig. 3. High-resolution Na 1 s XPS (a) and V 2p XPS (b) spectra for the V_2O_3 /a-NVO heterostructure; V L-edge XAS (c) and O K-edge XAS (d) spectra for the V_2O_3 /a-NVO heterostructure, V_2O_3 reference (data collecting from Reference 34) and $Na_{0.33}V_2O_5$ reference (data collecting from Reference 35).

relatively low polarization potential, indicating the quick Zn^{2+} ion insertion/extraction kinetics. The GCD curves of the V_2O_3/a-NVO electrode at different current densities are presented in Fig. 4c, where the discharge voltage plateaus at 0.6 V and 0.9 V, and the charge plateaus at 0.8 V and 1.1 V are observed, corresponding to the multiple Zn^{2+} ion insertion/extraction processes described in the CV curves. Fig. 4d shows the rate performance of V_2O_3/a-NVO and VO_2/NVO cathodes at current densities ranging from 0.2 to 20 A/g, where the V_2O_3/a-NVO heterostructure delivers the discharge capacities of 414.6, 390.4, 358.5, 305.5, 207.1, 121.2, 87.5, and 69.2 mAh/g at current densities of 0.2, 0.5, 1, 2, 5, 10, 15, and 20 A/g, respectively. In contrast, the discharge capacities of the VO_2/NVO cathode are 161.7, 142.3, 125.9, 107, 78.3, 58, 48.9, and 43 mAh/g at the same current densities. It is evident that the V_2O_3/a-NVO heterostructure exhibits higher rate performance. Notably, when the current density turns back to 0.2 A/g, the specific capacity of V_2O_3/a-NVO heterostructure recovers to 414 mAh/g, implying excellent reversibility. Further, the cycling performance of the V_2O_3/a-NVO and VO_2/NVO cathodes at a current density of 1 A/g was investigated. As shown in Fig. 4e, the V_2O_3/a-NVO electrode delivers a higher initial capacity of 367.9 mAh/g than that of the VO_2/NVO sample (71.8 mAh/g). After cycling for 1000 cycles, the discharge capacity of V_2O_3/a-NVO remains at 329.2 mAh/g with a capacity retention of 89 %, outperforming the VO_2/NVO electrode. For comparison, the cycling performance of commercial V_2O_5 and urea mixture sintered by the flash Joule heating and the NaCl-treated V_2O_5 without flash Joule heating were also evaluated. As displayed in Fig. S7, both samples exhibit more rapid decay in specific capacities compared to the V_2O_3/a-NVO cathode, strongly suggesting the superior electrochemical performance of the V_2O_3/a-NVO heterostructure and also highlighting the great potential of flash Joule heating in obtaining efficient vanadium oxide-based cathodes.

To optimize the electrochemical performance, the experimental conditions for fabricating the V_2O_3/a-NVO heterostructure were explored. As shown in Fig. S8a, the cycling performance at a current density of 1 A/g reveals that the sample synthesized with a 50 wt% urea precursor (i.e., the weight ratio of urea to sodium vanadate is 1:1) exhibits the optimal specific capacity. Additionally, the sintering temperature for the V_2O_3/a-NVO heterostructure achieved by flash Joule heating treatment has also been investigated. As presented in Fig. S8b, the sample prepared at 1600 °C delivers the highest specific capacity along with superior stability at a current density of 1 A/g. The long-term cycling performance at a high current density was also measured to evaluate the cycling stability of the resulting samples. As shown in Fig. 4f, at a high current density of 10 A/g, the V_2O_3/a-NVO electrode maintains a specific capacity of 138 mAh/g after 5000 cycles, while the VO_2/NVO electrode exhibits an obvious activation process followed by a rapid decline in specific capacity (Fig. 4g). These results strongly suggest the enhanced electrochemical performance of the V_2O_3/a-NVO electrode.

To get insights into the improved electrochemical performance of the V_2O_3/a-NVO electrode, electrochemical kinetics behaviors were evaluated by performing the measurements of CV at different scan rates, galvanostatic intermittent titration technique (GITT), and electrochemical impedance spectroscopy (EIS). Fig. 5a shows the CV curves at varying scan rates of 0.1, 0.2, 0.4, 0.6, 0.8, and 1.0 mV/s, aimed at investigating the diffusion control and surface capacitive of the V_2O_3/a-NVO electrode. Generally, the contributions of capacitance and diffusion can be determined by calculating the b value using Equation (1):

$$i = av^b \tag{1}$$

In which a and b are alterable parameters. Typically, the b value of 0.5 is indicative of a diffusion-controlled process, while a value close to 1.0 suggests a capacitive-controlled behavior [40,41]. Based on the log(i) versus log(v) plots shown in Fig. 5b, the fitted b-values for peaks 1, 2, 3, and 4 for the V_2O_3/a-NVO electrode were found to be 0.90, 0.67, 0.66, and 0.94, respectively. It manifests that the charge storage process in the V_2O_3/a-NVO electrode is predominantly dominated by the surface pseudo-capacitive process, which is mainly because abundant storage sites and isotropic charge transfer channels of a-NVO as well as the

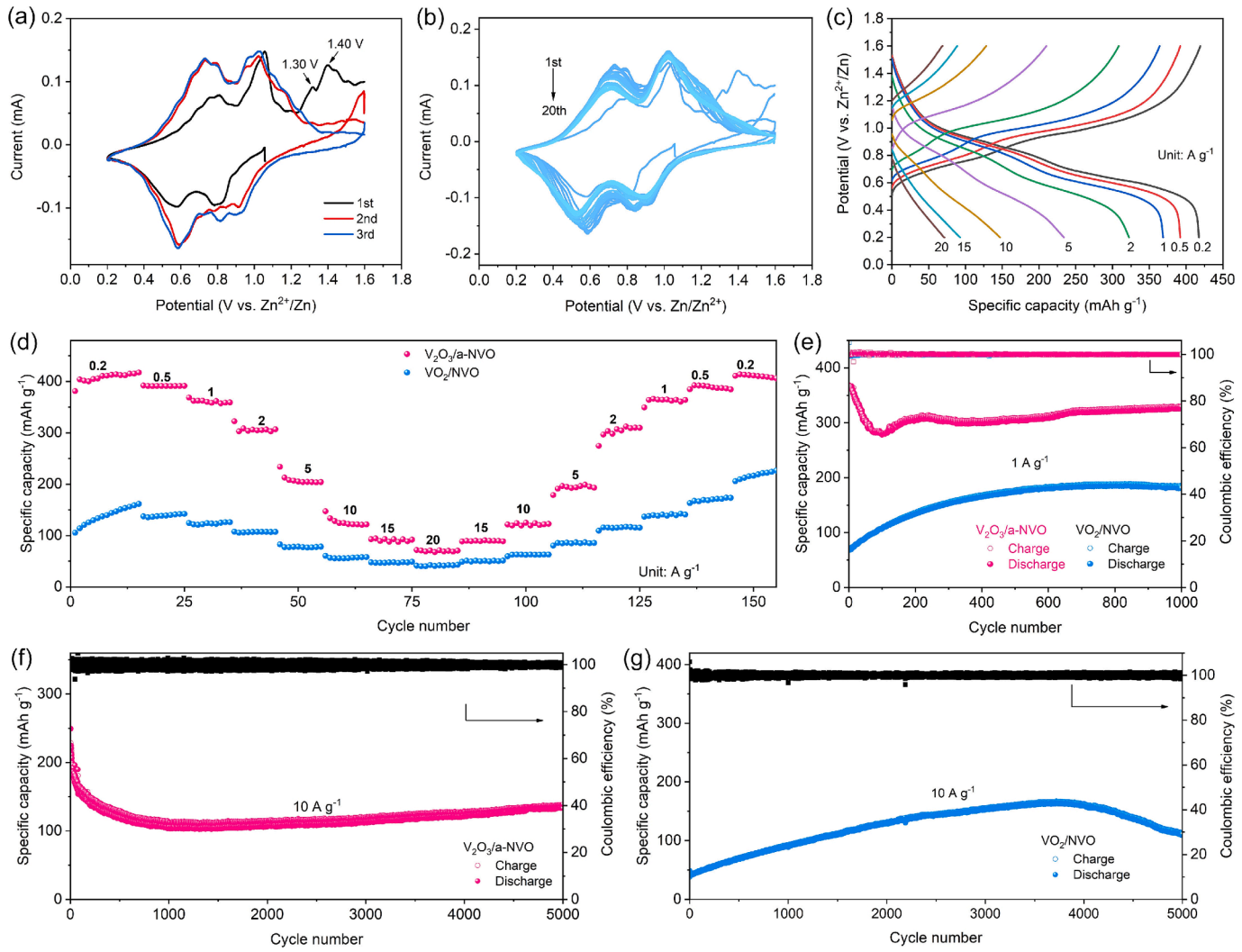

Fig. 4. CV curves for the initial three cycles (a) and 20 cycles (b) of the V_2O_3 /a-NVO cathode, GCD curves of the V_2O_3 /a-NVO cathode at different current densities (c), rate performance (d), and cycling performance at 1 A/g (e) of V_2O_3 /a-NVO and VO_2 /NVO cathodes, and long-term cycling at 10 A/g for the V_2O_3 /a-NVO (f) and VO_2 /NVO (g) cathodes.

intimate contact between crystalline V_2O_3 and a-NVO, greatly facilitating rapid charge transfer and enhancing the electrochemical reaction kinetics. Further assessment of the contributions from surface pseudocapacitance and diffusion control was performed using Equation (2).

$$i = k_1 v + k_2 v^{1/2} \tag{2}$$

Where k_1v and $k_2v^{1/2}$ represent current contributions resulting from surface capacitive effects and diffusion-controlled processes, respectively [40,41]. As shown in Fig. 5c, the capacitive-controlled contribution rises with increasing scan rates from 0.2 to 1 mV/s. Remarkably, a capacitive contribution of 94.9 % of the total current (capacity) is observed at a scanning rate of 1.0 mV/s (Fig. 5d). These findings further confirm that the electrochemical reactions in the V_2O_3/a-NVO electrode are primarily dominated by capacitive processes, especially at high current densities, which favor enhanced electron transfer kinetics and contribute to a high rate capability [40,41].

To further explore the reaction kinetics of the V_2O_3/a-NVO electrode, EIS and GITT measurements were conducted to better understand the underlying causes for the enhanced electrochemical performance. The Nyquist plots of the V_2O_3/a-NVO and VO_2/NVO electrodes are presented in Fig. 5e, where a smaller radius in the high-frequency region is clearly observed for the V_2O_3/a-NVO sample. Fig. S9 shows the equivalent circuit used for simulating the Nyquist plots, and the fitting results reveal a lower charge transfer resistance (R_{ct}) of 151.4 Ω for the V_2O_3/a-NVO than that of the VO_2/NVO (589 Ω) electrode. This indicates enhanced charge transfer kinetics owing to the amorphous nature of a-NVO in the as-obtained heterostructure [42–44]. Subsequently, GITT tests (Fig. S10) were performed to quantitatively analyze the diffusion coefficient (D_{Zn}^{2+}) of Zn^{2+} of the V_2O_3/a-NVO electrode. The results, shown in Fig. 5f, indicate that the calculated D_{Zn}^{2+} values for the V_2O_3/a-NVO electrode range between 10^{-9} and 10^{-11} cm^2 S^{-1}, which is obviously higher than that of the VO_2/NVO electrode, consistent with the EIS results. All these results manifest that the charge kinetics in the V_2O_3/a-NVO heterostructure are significantly enhanced, likely due to rich storage sites and isotropic ions diffusion routes of a-NVO as well as the intimate contact between V_2O_3 and a-NVO.

To understand the storage mechanism of the V_2O_3/a-NVO electrode, ex-situ XRD characterizations were carried out to investigate the structural evolution during charge and discharge states. As shown in Fig. 6a, an addition diffraction peak at ~ 8° is observed for the sample after the standing period (labeled as 'A'), and its intensity gradually increases during the discharge process of the first cycle, which can be attributed to the formation of a new phase of $Zn_4(OH)_6SO_4{\cdot}5H_2O$ (ZHS, PDF: #78–0246). Typically, the newly assembled cell undergoes an electrolyte infiltration process during the standing period, in which the open-circuit voltage will drop rapidly and greatly due to the self-discharge

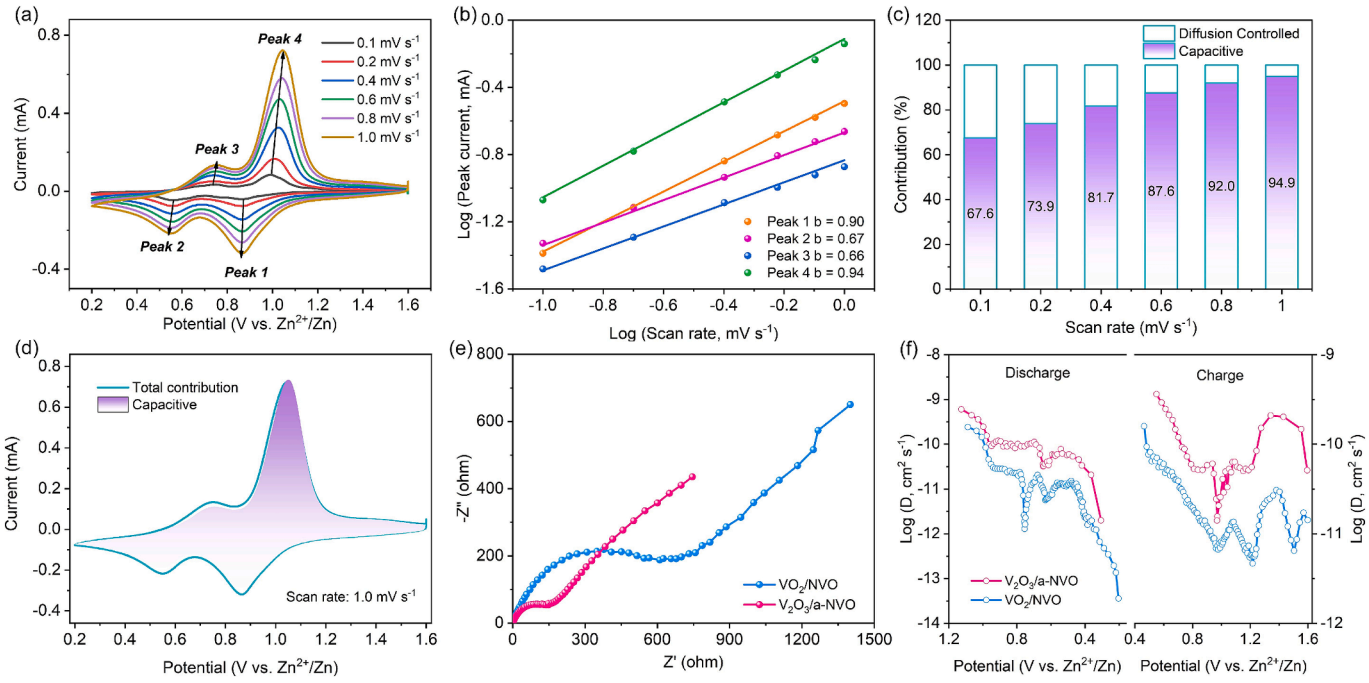

Fig. 5. (a) CV curves of V_2O_3 /a-NVO at various scan rates ranging from 0.1 to 1.0 mV/s , (b) log(i) versus log(v) curves of cathodic and anodic peaks, (c) the capacitive and diffusion-controlled contributions to capacity at different scan rates, (d) capacitive contribution to charge storage at 1 mV/s , (e) EIS spectra of the VO_2 /NVO and V_2O_3 /a-NVO electrodes before cycling, (f) the calculated diffusion coefficients of the VO_2 /NVO and V_2O_3 /a-NVO electrodes.

reaction [37]. This reaction leads to the decomposition of water, generating abundant H^+ ions that insert into the layered structure of host materials. Concurrently, an equivalent amount of OH^- ions is produced and reacts with $Zn(CF_3SO_3)_2$ in the electrolyte to form ZHS [37,45,46]. This implies that the formation of ZHS is related to the intercalation of H^+ ions into the layered structure of host materials. The generation of ZHS during the discharge process of the first cycle is further evidenced by ex-situ SEM and XPS characterizations. As presented in Fig. S11a and Fig. S11b, the SEM image clearly reveals that numerous ZHS flakes are generated on the electrode surface at the fully discharged state (0.2 V vs. Zn/Zn^{2+}). Fig. 6e displays the high-resolution O 1 s XPS spectra at different states, where the presence of OH^- species originating from ZHS is observed in the spectrum at the fully discharged state. Fig. 6b displays the XPS survey spectra of the V_2O_3/a-NVO cathode at the full discharge/charge states of the first cycle, where Na 1 s XPS signal vanishes (Fig. 6c) while a distinct Zn 2p peak is detected (Fig. 6d), suggesting the generation of ZHS and the displacement of Na^+ ions due to the H^+ insertion. Furthermore, ex-situ XRD patterns (Fig. 6a) have shown that the peak positions for the V_2O_3 phase are unchanged throughout the electrochemical process of the first cycle but the peak intensities gradually decrease and completely disappear at the full discharge state (0.2 V vs. Zn^{2+}/Zn). Generally, the intercalation of multivalent Zn^{2+} into vanadium oxides could result in the strong deformation of the crystal structure, therefore the similar diffraction peak positions for V_2O_3 rule out the possibility of the multivalent Zn^{2+} insertion into the V_2O_3/a-NVO cathode [47]. Further, during the charging process of the first cycle, the diffraction peaks of ZHS gradually diminish, and the flake-like morphologies also completely vanish after full charging (1.6 V vs. Zn/Zn^{2+}, SEM image in Fig. S11c and Fig. S11d), indicating the highly reversible phase transition. At the same time, the formation of $VO_2{\cdot}0.5H_2O$ (PDF: #01–089-6930) phase has been found owing to the deintercalation of H^+ ions. Fig. 6a also presents the ex-situ XRD patterns of V_2O_3/a-NVO heterostructure after the 20th cycle, further supporting the reversible formation of ZHS. Concurrently, a new phase of $Zn_3(OH)_2V_2O_7{\cdot}2H_2O$ (ZVOH, PDF: #50–0570) emerges in the charging process and then gradually decreases and disappears, suggesting the reversible conversion of the ZVOH phase [48]. Moreover, besides the peaks from ZHS and ZVOH, no other peaks related to crystalline V-based compounds are observed throughout the electrochemical processes, manifesting the amorphous transformation process of the V_2O_3/a-NVO heterostructure caused by the H^+ insertion/desertion [46,49]. Overall, based on the above analysis, the storage kinetics of V_2O_3/a-NVO heterostructure can be outlined as below:

The first few cycles:

Discharge:

$$H_2O \rightarrow H^+ + OH^-$$

$$V_2O_3 + NVO(amorphous) + H^+ + e^- \rightarrow H_{insert}VO_x$$

$$Zn^{2+} + OH^- + Zn(CF_3SO_3)_2 + H_2O \rightarrow Zn_4SO_4(OH)_6 \bullet 5H_2O$$

Charge:

$$Zn_4SO_4(OH)_6 \bullet 5H_2O + H_{insert}VO_x \rightarrow VO_2 \bullet 5H_2O + Zn^{2+} + H^+ + SO_4^{2-} + e^-$$

The subsequent cycles:

$$Zn_4SO_4(OH)_6 \bullet 5H_2O + H_{insert}VO_x \rightarrow Zn_3(OH)_2V_2O_7 \bullet 2H_2O + Zn^{2+} + H^+ + SO_4^{2-} + e^-$$

The reaction on the zinc anode:

$$Zn \leftrightarrow Zn^{2+} + 2e^-$$

4. Conclusions

An amorphous-crystalline V_2O_3/a-NVO heterostructure was rapidly constructed using a facile and cost-effective flash Joule heating method. When employed as the cathode for ZIBs, this heterostructure delivers impressive electrochemical performance, achieving a high specific capacity of 414.6 mAh/g at a current density of 0.2 A/g and maintaining 329.2 mAh/g after 1000 cycles at 1 A/g, with a capacity retention rate of 89 %. Additionally, it demonstrates a remarkable long-term cycling stability of 138 mAh/g after 5000 cycles at 10 A/g. The formation of the

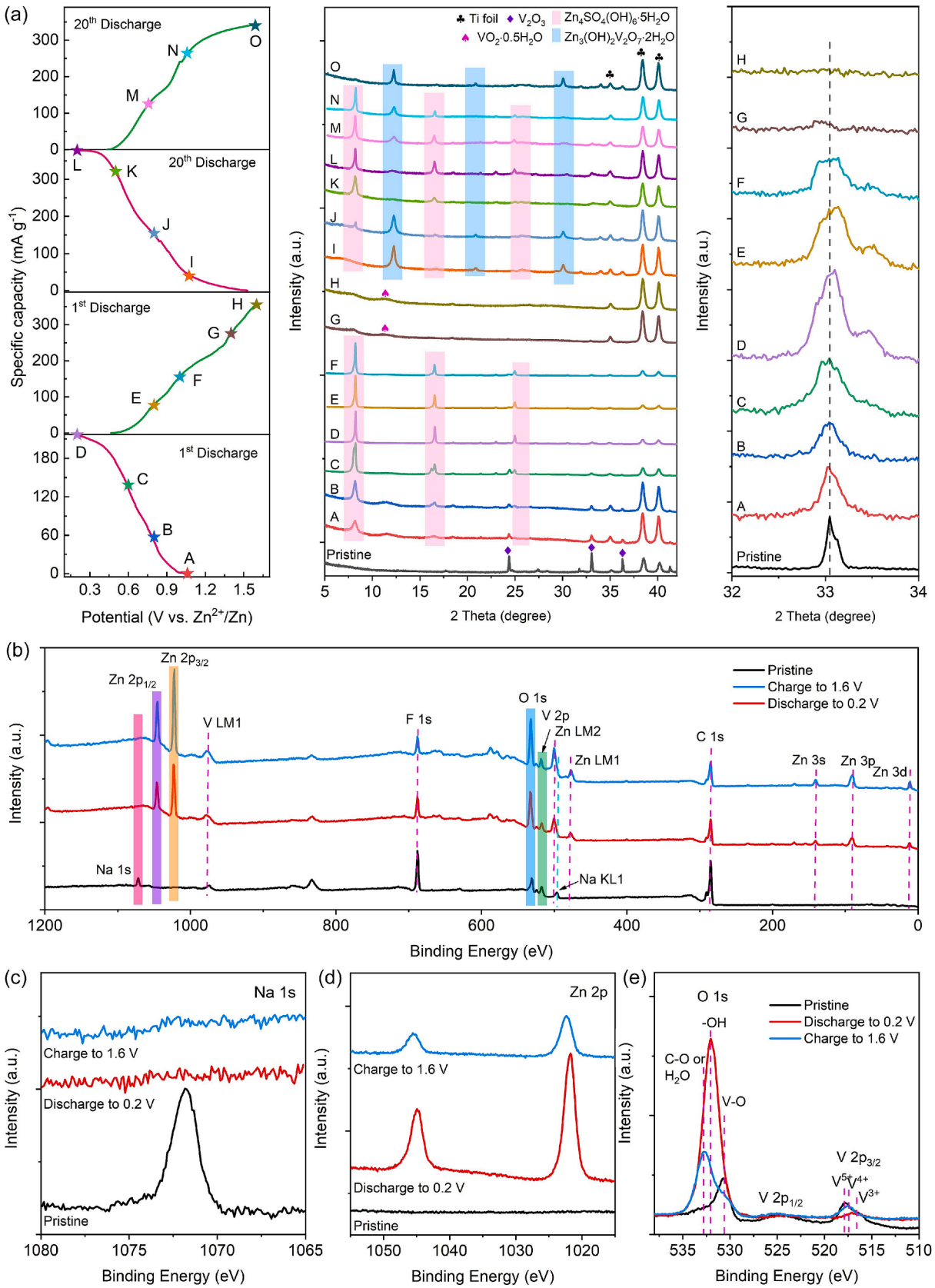

Fig. 6. (a) Ex-situ XRD patterns of V_2O_3 /a-NVO cathodes at charge/discharge states for the 1st and 20th cycles, (b) survey, (c) Na 1 s, (d) Zn 2p, (e) O 1 s and V 2p ex-situ XPS spectra of V_2O_3 /a-NVO cathodes at different charge/discharge states for the 1st cycle.

amorphous NVO phase provides more Zn^{2+} storage sites and isotropic charge transfer channels, which combined with the intimate contact between crystalline V_2O_3 and a-NVO greatly facilitate the reaction kinetics and pseudocapacitive contributions. Moreover, the co-intercalation of H^+/Zn^{2+} further accelerates charge dynamics, thereby boosting electrochemical performance. This work provides a viable strategy for the design of efficient vanadium-based cathodes for aqueous ZIBs.

CRediT authorship contribution statement

Duan Yan: Methodology, Data curation. **Hanbo Li:** Methodology, Data curation. **Aomen Yang:** Methodology, Data curation. **Menglian Wang:** Methodology, Data curation. **Kaiqi Nie:** Methodology, Data curation. **Xiaoxin Lv:** Writing – review & editing, Writing – original draft, Supervision, Project administration. **Jiujun Deng:** Writing – review & editing, Writing – original draft, Supervision, Funding acquisition.

Declaration of competing interest

The authors declare that they have no known competing financial interests or personal relationships that could have appeared to influence the work reported in this paper.

Acknowledgments

We acknowledge the financial support from Jiangsu University Foundation (18JDG019) and National Natural Science Foundation of China (51902139).

Appendix A. Supplementary data

The calculation method of Zn^{2+} diffusion coefficient, heating/quenching curve, XRD patterns, XPS spectra, SEM image, Raman spectra, TGA curve, cycling performance, and GITT plots. Supplementary data to this article can be found online at https://doi.org/10.1016/j.cej.2024.158966.

Data availability

Data will be made available on request.

References

[1] Y. Liang, Y. Yao, Designing modern aqueous batteries, Nat. Rev. Mater. 8 (2023) 109–122.
[2] Z. Liu, Y. Huang, Y. Huang, Q. Yang, X. Li, Z. Huang, C. Zhi, Voltage issue of aqueous rechargeable metal-ion batteries, Chem. Soc. Rev. 49 (2020) 180–232.
[3] B. Tang, L. Shan, S. Liang, J. Zhou, Issues and opportunities facing aqueous zinc-ion batteries, Energy Environ. Sci. 12 (2019) 3288–3304.
[4] C. Li, S. Jin, L.A. Archer, L.F. Nazar, Toward practical aqueous zinc-ion batteries for electrochemical energy storage, Joule 6 (2022) 1733–1738.
[5] Q. Song, S. Zhou, S. Wang, S. Li, L. Xu, J. Qiu, Insights into the oxygen vacancies in transition metal oxides for aqueous Zinc-Ion batteries, Chem. Eng. J. 461 (2023) 142033.
[6] G. Li, L. Sun, S. Zhang, C. Zhang, H. Jin, K. Davey, G. Liang, S. Liu, J. Mao, Z. Guo, Developing Cathode Materials for Aqueous Zinc Ion Batteries: Challenges and Practical Prospects, Adv. Funct. Mater. 34 (2024) 2301291.
[7] X. Wang, Z. Zhang, B. Xi, W. Chen, Y. Jia, J. Feng, S. Xiong, Advances and Perspectives of Cathode Storage Chemistry in Aqueous Zinc-Ion Batteries, ACS Nano 15 (2021) 9244–9272.
[8] K. Zhu, W. Yang, Vanadium-Based Cathodes for Aqueous Zinc-Ion Batteries: Mechanisms, Challenges, and Strategies, Acc. Chem. Res. 57 (2024) 2887–2900.
[9] N. Liu, B. Li, Z. He, L. Dai, H. Wang, L. Wang, Recent advances and perspectives on vanadium- and manganese-based cathode materials for aqueous zinc ion batteries, J. Energy Chem. 59 (2021) 134–159.
[10] S. Pavithra, K. Pramoda, R.S. Keri, Performance of nanostructured zinc vanadates for energy storage applications: Current status and future perspectives, Chem. Eng. J. 495 (2024) 153423.
[11] Z. Wang, Y. Song, J. Wang, Y. Lin, J. Meng, W. Cui, X.-X. Liu, Vanadium Oxides with Amorphous-Crystalline Heterointerface Network for Aqueous Zinc-Ion Batteries, Angew. Chem., Int. Ed. 62 (2023) e202216290.
[12] W. Wang, Y. Ouyang, J. Yan, R. Hu, C. Zhang, A stepwise oxidation strategy for the synthesis of amorphous V_2O_5@V_2CT_x nanohybrid cathodes toward high-performance aqueous Zn-ion batteries, J. Mater. Chem. A 11 (2023) 8224–8234.
[13] C. Hu, B. Li, K. Nie, Z. Wang, Y. Zhang, L. Yi, X. Hao, H. Zhang, S. Chong, Z. Liu, W. Huang, Ultrafast Tailoring Amorphous $Zn_{0.25}V_2O_5$ with Precision-Engineered Artificial Atomic-Layer 1T′-MoS_2 Cathode Electrolyte Interphase for Advanced Aqueous Zinc-Ion Batteries, Angew. Chem., Int. Ed. (2024) e202413173.
[14] C. Huang, C. Wu, Z. Zhang, Y. Xie, Y. Li, C. Yang, H. Wang, Crystalline and amorphous MnO_2 cathodes with open framework enable high-performance aqueous zinc-ion batteries, Front, Mater. Sci. 15 (2021) 202–215.
[15] B. Jia, B. Zhang, Z. Cai, X. Yang, L. Li, L. Guo, Construction of amorphous/crystalline heterointerfaces for enhanced electrochemical processes, eScience 3 (2023) 100112.
[16] Z. Gong, J. Liu, G. Ye, H. Fei, Amorphous/crystalline heterophase electrocatalysts: synthesis, applications and perspectives, Chem. Commun. 59 (2023) 5661–5676.
[17] H. Lan, J. Wang, L. Cheng, D. Yu, H. Wang, L. Guo, The synthesis and application of crystalline-amorphous hybrid materials, Chem. Soc. Rev. 53 (2024) 684–713.
[18] K.M. Wyss, D.X. Luong, J.M. Tour, Large-Scale Syntheses of 2D Materials: Flash Joule Heating and Other Methods, Adv. Mater. 34 (2022) 2106970.
[19] J. Yuan, Y. Zhang, F. Chen, Z. Gu, An overview of Joule heating in energy storage materials and applications, J. Mater. Chem. C 12 (2024) 14729–14753.
[20] X. Ding, Z. He, J. Li, X. Xu, Z. Li, Carbon carrier-based rapid Joule heating technology: a review on the preparation and applications of functional nanomaterials, Nanoscale 16 (2024) 12309–12328.
[21] P. Huang, Z. Li, L. Chen, Y. Li, Z. Liu, J. Zhang, J. Luo, W. Zhang, W.-D. Liu, X. Zhang, R. Zhu, Y. Chen, Ultrafast Dual-Shock Chemistry Synthesis of Ordered/Disordered Hybrid Carbon Anodes: High-Rate Performance of Li-Ion Batteries, ACS Nano 18 (2024) 18344–18354.
[22] X. Lv, A. Yang, M. Wang, K. Nie, J. Deng, X. Sun, Flash Joule Heating Synthesis of Layer-Stacked Vanadium Oxide/Graphene Hybrids within Seconds for High-Performance Aqueous Zinc-Ion Batteries, ACS Appl. Mater. Interfaces 16 (2024) 52290–52298.
[23] S. Park, S. Woo, J. Kim, J. Lee, H. Lee, K.-M. Kim, J. Ahn, H.-T. Kim, Y.J. Kim, J. Kim, I.-D. Kim, S.-J. Kim, A Joule-heating-derived multiphase porous TiO_2 support for reinforcing high-entropy alloy catalysts, Chem. Eng. J. 493 (2024) 152551.
[24] Y. Yao, Z. Huang, P. Xie, L. Wu, L. Ma, T. Li, Z. Pang, M. Jiao, Z. Liang, J. Gao, Y. He, D. J. Kline, M. R. Zachariah, C. Wang, J. Lu, T. Wu, T. Li, C. Wang, R. S.-Yassar, L. Hu, High temperature shockwave stabilized single atoms. Nat. Nanotechnol. 14 (2019) 851-857.
[25] J. Deng, G. Li, D. Yan, W. Zhang, K. Feng, K. Nie, C. Liu, X. Lv, J. Zhong, Programmable Wet-Interfacial Joule Heating to Rapidly Synthesize Metastable Protohematite Photoanodes: Metal and Lattice Oxygen Dual Sites for Improving Water Oxidation, ACS Catal. 14 (2024) 10635–10647.
[26] X. Cui, Y. Liu, Y. Chen, Ultrafast micro/nano-manufacturing of metastable materials for energy, Natl. Sci. Rev. 11 (2024) nwae033.
[27] I.N. Reddy, A. Sreedhar, C.V. Reddy, M. Cho, D. Kim, J. Shim, Facile synthesis and characterization of V_2O_5 nanobelt bundles containing plasmonic Ag for photoelectrochemical water splitting under visible light irradiation, Ceram. Int. 45 (2019) 23333–23340.
[28] X. Shan, S. Kim, A. M. M. Abeykoon, Gi. Kwon, D. Olds, X. Teng, Potentiodynamics of the Zinc and Proton Storage in Disordered Sodium Vanadate for Aqueous Zn-Ion Batteries, ACS Appl. Mater. Interfaces 12 (2020) 54627-54636.
[29] H. Lu, Z. Zhang, X. An, J. Feng, S. Xiong, B. Xi, In Situ Electrochemically Transforming VN/V_2O_3 Heterostructure to Highly Reversible V_2NO for Excellent Zinc Ion Storage, Small Struct. 4 (2023) 2300191.
[30] X. Pan, G. Ren, M.N.F. Hoque, S. Bayne, K. Zhu, Z. Fan, Fast Supercapacitors Based on Graphene-Bridged V_2O_3/VO_x Core-Shell Nanostructure Electrodes with a Power Density of 1 MW kg^1, Adv. Mater. Interfaces 1 (2014) 1400398.
[31] J. Wu, H. Liang, J. Li, Z. Yang, J. Cai, Facile preparation of urchin-like morphology V_2O_3-VN nano-heterojunction cathodes for high-performance Aqueous zinc ion battery, J. Colloid Interface Sci. 654 (2024) 46–55.
[32] S. Wei, Y. Wang, S. Chen, L. Song, Structure regulation and synchrotron radiation investigation of cathode materials for aqueous Zn-ion batteries, Chem. Sci. 15 (2024) 7848–7869.
[33] X. Lv, G. Li, G. Zhang, K. Feng, J. Deng, J. Zhong, Soft X-Ray Absorption Spectroscopy of Advanced Two-Dimensional Photo/Electrocatalysts for Water Splitting, Chin. J. Struct. Chem. 41 (2022) 2210016–2210028.
[34] A. Jana, R.J. Choudhary, D.M. Phase, Mott-Hubbard type insulating nature of epitaxial $LaVO_3$ thin films, Phys. Rev. B 98 (2018) 075124.
[35] B. Chen, J. Laverock, D. Newby Jr., T.-Y. Su, K.E. Smith, W. Wu, L.H. Doerrer, N. F. Quackenbush, S. Sallis, L.F.J. Piper, D.A. Fischer, J.C. Woicik, Electronic Structure of β-$Na_xV_2O_5$ (x≈0.33) Polycrystalline Films: Growth, Spectroscopy, and Theory, J. Phys. Chem. C 118 (2014) 1081–1094.
[36] X. Wang, Z. Zhang, M. Huang, J. Feng, S. Xiong, B. Xi, In Situ Electrochemically Activated Vanadium Oxide Cathode for Advanced Aqueous Zn-Ion Batteries, Nano Lett. 22 (2022) 119–127.
[37] H. Luo, B. Wang, F. Wu, J. Jian, K. Yang, F. Jin, B. Cong, Y. Ning, Y. Zhou, D. Wang, H. Liu, S. Dou, Synergistic nanostructure and heterointerface design propelled ultra-efficient in-situ self-transformation of zinc-ion battery cathodes with favorable kinetics, Nano Energy 81 (2021) 105601.

[38] C. Liu, M. Tian, M. Wang, J. Zheng, S. Wang, M. Yan, Z. Wang, Z. Yin, J. Yang, G. Cao, Catalyzing Zinc-ion Intercalation in Hydrated Vanadates for Aqueous Zinc-ion Batteries, J. Mater. Chem. A 8 (2020) 7713–7723.
[39] Z. Wang, P. Cui, X. Wang, M. Chang, Y. Yu, J. You, F. Hu, Y. Wu, K. Zhu, Co-Substitution Engineering Boosting the Kinetics and Stability of VO_2 for Zn Ion Batteries, Adv. Funct. Mater. 2407925 (2024).
[40] C. Gao, W. Sun, W. Zhang, Q. Zhang, S. Guang, Q. Chen, In-situ electrochemical conversion of V_2O_3@C into $Zn_3(OH)_2V_2O_7{\cdot}2H_2O$@C for high-performance aqueous Zn-ion batteries, J. Power Sources 613 (2024) 234942.
[41] Z. Pang, B. Ding, J. Wang, Y. Wang, L. Xu, L. Zhou, X. Jiang, X. Yan, J.P. Hill, L. Yu, Y. Yamauchi, Metal-ion inserted vanadium oxide nanoribbons as high-performance cathodes for aqueous zinc-ion batteries, Chem. Eng. J. 446 (2022) 136861.
[42] Z. Zhou, M. Han, Y. Sun, Y. Cui, S.A. El-khodary, D.H.L. Ng, J. Lian, J. Ma, Zinc-Ion and Proton as Joint Charge Carriers of S-MoO_2 for High-Capacity Aqueous Zinc-Ion Batteries, Adv. Funct. Mater. 34 (2024) 2308834.
[43] X. Wang, Y. Li, S. Wang, F. Zhou, P. Das, C. Sun, S. Zheng, Z.-S. Wu, 2D Amorphous V_2O_5/Graphene Heterostructures for High-Safety Aqueous Zn-Ion Batteries with Unprecedented Capacity and Ultrahigh Rate Capability, Adv. Energy Mater. 10 (2020) 2000081.
[44] Y. Zhang, Z. Li, M. Liu, J. Liu, Construction of novel polyaniline-intercalated hierarchical porous V_2O_5 nanobelts with enhanced diffusion kinetics and ultra-stable cyclability for aqueous zinc-ion batteries, Chem. Eng. J. 463 (2023) 142425.
[45] W. Zhong, J. Zhang, Z. Li, Z. Shen, S. Zhang, X. Wang, Y. Lu, Issues and strategies of cathode materials for mild aqueous static zinc-ion batteries, Green, Chem. Eng. 4 (2023) 264–284.
[46] Y. Cai, R. Chua, S. Huang, H. Ren, M. Srinivasan, Amorphous manganese dioxide with the enhanced pseudocapacitive performance for aqueous rechargeable zinc-ion battery, Chem. Eng. J. 396 (2020) 125221.
[47] Z. Li, S. Ganapathy, Y. Xu, Z. Zhou, M. Sarilar, M. Wagemaker, Mechanistic Insight into the Electrochemical Performance of Zn/VO_2 Batteries with an Aqueous $ZnSO_4$ Electrolyte, Adv. Energy Mater. 9 (2019) 1900237.
[48] K. Yang, Y. Hu, L. Li, L. Cui, L. He, S. Wang, J. Zhao, Y.-F. Song, First high-nuclearity mixed-valence polyoxometalate with hierarchical interconnected Zn^{2+} migration channels as an advanced cathode material in aqueous zinc-ion battery, Nano Energy 74 (2020) 104851.
[49] D. Li, Z. Ye, H. Ding, J. Li, H. Huang, Z. Yang, J. Su, J. Zhu, W. Zhang, Boosting proton intercalation via sulfur anion doping in V_2O_3 cathode materials towards high capacity and rate performance of aqueous zinc ion batteries, Energy Storage Mater. 71 (2024) 103635.